Finite Element Approximation of the Acoustic Wave Equation: Error Control and Mesh Adaptation

Wolfgang Bangerth and Rolf Rannacher

Institute for Applied Mathematics,
University of Heidelberg, Germany
wolfgang.bangerth@iwr.uni-heidelberg.de
rannacher@iwr.uni-heidelberg.de

This paper appeared in
East-West Journal of Numerical Mathematics
Volume 7, Number 4 (1999), pages 263–282

Finite Element Approximation of the Acoustic Wave Equation: Error Control and Mesh Adaptation

Wolfgang Bangerth and Rolf Rannacher[1]

Institute for Applied Mathematics,
University of Heidelberg, Germany
wolfgang.bangerth@iwr.uni-heidelberg.de
rannacher@iwr.uni-heidelberg.de

Abstract

We present an approach to solving the acoustic wave equation by adaptive finite element methods. Using a global duality argument and Galerkin orthogonality, we obtain a residual-based error representation with respect to an arbitrary functional of the solution. This results in numerically evaluatable error estimates which are used for mesh refinement. In this way, very economical and highly localized space-time meshes can be generated which are tailored to the efficient computation of the quantity of interest. We demonstrate the performance and some of the mechanisms acting in our approach by numerical examples.

1 Introduction

We consider the acoustic wave equation

$$\begin{aligned} \rho(\mathbf{x})\partial_t^2 u(\mathbf{x},t) - \nabla\cdot a(\mathbf{x})\nabla u(\mathbf{x},t) &= 0 && (\mathbf{x},t)\in Q_T=\Omega\times I,\\ u(\mathbf{x},0)=u^0(\mathbf{x}),\qquad \partial_t u(\mathbf{x},0)&=v^0(\mathbf{x}) && \mathbf{x}\in\Omega, \\ \mathbf{n}\cdot a(\mathbf{x})\nabla u(\mathbf{x},t) &= 0 && (\mathbf{x},t)\in\Gamma\times I,\Gamma=\partial\Omega. \end{aligned} \tag{1}$$

on a space-time region $Q_T := \Omega \times I$, where $\Omega \subset \mathbb{R}^d$, $d \geq 1$, and $I = (0,T)$; density ρ and elastic coefficient a may vary in space. This equation frequently occurs in the simulation of acoustic waves in gaseous or fluid media, seismics, electrodynamics and many other applications. In many cases, initial data and coefficients are rough or discontinuous which limits the global regularity of solutions.

Since solutions to the wave equation often have very localized features, such as wave fronts, it is widely recognized that efficient algorithms need to employ some kind of adaptivity in the choice of computational grids. On the other hand, the quantities one is interest in from an engineering viewpoint also are often local rather than global. It is therefore not always necessary to resolve all features of a wave field, if one is only interested in a certain portion. Adaptivity should therefore take into account both kinds of localization.

Despite the common perception that adaptivity is crucial to the efficient solution of the wave equation, there does not exist much literature on *a posteriori* error estimates and practical implementations (see, e.g., Johnson [17], and Li and Wiberg [20]). However, there

[1]The authors acknowledge the support by the German Research Association (DFG) through the Graduiertenkolleg and the SFB 359 at the IWR, Universität Heidelberg.

exists significant work on *a priori* estimates for the wave equation (see, among many others, Hulbert and Hughes [16], Hulbert [15], Johnson [17], Bales and Lasiecka [1], French and Peterson [12]). Furthermore, goal-oriented a posteriori error estimation has been developed for other equations than the wave equation (see Eriksson and Johnson [11], Eriksson, et al. [10], Hartmann [14], Kanschat [18], Peraire and Patera [22], Oden and Prudhomme [21], and [7, 6, 23]).

The main aim of this work is to derive residual-based a posteriori error representations for the numerical solution of the wave equation. The local cell residuals are multiplied by weights involving the solution of a global dual problem, which is adjusted to the quantity of interest. While the residuals depend on the local regularity of the solution, the weights carry information about the properties of the quantity of interest. By evaluating the error representation on the space-time cells of the finite element mesh, we obtain local error indicators which are used for mesh adjustment. In several examples, we will demonstrate the advantage of the approach proposed in this work over other refinement strategies based on ad hoc criteria.

The outline of this paper is as follows. In the rest of this section, we will state the continuous formulation of the problem, while in the next section, our method of discretization of this formulation will be explained. In Section 3, we derive error estimates with respect to arbitrary functionals of the solution based on duality arguments involving the residuals of the numerical solution. The practical evaluation of this new *weighted* error estimator is discussed in some detail. Global norm a posteriori estimates based on duality arguments have already been derived by Johnson [17] for the discontinuous-in-time Galerkin approximation of the wave equation. We will present numerical examples of computations with the proposed methods in Section 4 and will conclude in Section 5.

1.1 The continuous problem

We will solve eq. (1) by a "velocity-displacement" formulation which is obtained by introducing a new velocity variable $v = \partial_t u$. The corresponding weak formulation in space-time is then obtained by multiplying by test functions $\boldsymbol{\tau}$ from a "test space" T, integrating by parts in space and imposing initial values $\mathbf{w}^0 = \{u^0, v^0\}$ in a weak sense: Find $\mathbf{w} = \{u, v\} \in W$, such that

$$a(\mathbf{w}, \boldsymbol{\tau}) = (\rho \mathbf{w}^0, \boldsymbol{\tau}(0))_\Omega \qquad \forall \boldsymbol{\tau} = \{\varphi, \psi\} \in T, \tag{2}$$

with the bilinear form

$$a(\mathbf{w}, \boldsymbol{\tau}) = (\rho \partial_t \mathbf{w}, \boldsymbol{\tau})_{Q_T} + \left(\begin{pmatrix} 0 & -\rho \\ a\nabla & 0 \end{pmatrix} \mathbf{w}, \begin{pmatrix} 1 & 0 \\ 0 & \nabla \end{pmatrix} \boldsymbol{\tau} \right)_{Q_T} + (\rho \mathbf{w}(0), \boldsymbol{\tau}(0))_\Omega . \tag{3}$$

The natural solution space is $W := H^1(I, H^1(\Omega)) \times H^1(I, L_2(\Omega))$. For T we choose a subset of $L_2(I, L_2(\Omega)) \times L_2(I, H^1(\Omega))$ which consists of functions right-continuous in time. We do so in order to retain a well-defined weak enforcement of initial values in (2). Clearly, the uniquely determined "strong" solution of (1) satisfies the variational equation.

This formulation of the wave equation, but without weak enforcement of initial values, and discretizations thereof were investigated in Hulbert and Hughes [16], Bales and Lasiecka [1], and French and Peterson [12] in the past; in the works by Hulbert [15], Johnson [17], and Li and Wiberg [20], a variant is used where the definition of the velocity, $v = \partial_t u$, is not enforced in the L_2 sense, but in H^1; weak enforcement of initial values would need to be

adjusted in this case as well. We chose the first formulation to take into account the case of reduced regularity.

For the formulation as chosen above, it is standard to show the following a priori equality which is obtained by testing (2) with $\boldsymbol{\tau} = \{\rho^{-1}\nabla\cdot a\nabla u, v\}\chi_{[0,t')}(t)$, with χ being the characteristic function of the time interval $[0,t')$ and $0 < t' \le T$:

$$\left\|\sqrt{\rho}v(t')\right\|_\Omega^2 + \left\|\sqrt{a}\nabla u(t')\right\|_\Omega^2 = \left\|\sqrt{\rho}v^0\right\|_\Omega^2 + \left\|\sqrt{a}\nabla u^0\right\|_\Omega^2. \tag{4}$$

Here we have used that the weak enforcement of initial values guarantees $\mathbf{w}(0) = \mathbf{w}^0$. This implies that any "weak" solution in the sense of (2) coincides with the "strong" solution given by (1). In view of the possibly missing smoothness of ρ and a the degree of regularity of the solution expressed by the identity (4) may be maximal. We will restrict our discussion of a posteriori error estimates to this natural situation.

Here and throughout the paper, we will use the notation

$$(\varphi,\psi)_\Omega = \int_\Omega \varphi\psi \; dx, \qquad (\varphi,\psi)_{Q_T} = \int_{Q_T} \varphi\psi \; dx \; dt,$$

for L_2 scalar products; $\|\varphi\|_S = (\varphi,\varphi)_S^{1/2}$ is the L_2 norm on some domain S. We also use the obvious extension to vector valued functions.

2 Discretization

To discretize problem (2), we use the so–called Rothe approach of first discretizing in time and then in space on each discrete time level. This has the advantage of having the freedom to choose the computational mesh differently at each time level. We subdivide the time interval $I = (0,T)$ into time slabs $I_n = (t_{n-1}, t_n)$ with length $k_n = t_n - t_{n-1}$. With each t_n, we associate decompositions $\mathbb{T}^n$ of Ω into (open) quadrilaterals ($d = 2$) or hexahedra ($d = 3$) satisfying the usual condition of shape regularity (see, e.g., Ciarlet [9]); to ease local mesh refinement and coarsening, we allow one "hanging node" per edge or face. We will denote cells by the symbol K and their diameter by h_K. For simplicity, we assume Ω to be a polygonal or polyhedral domain.

The time semi-discretization is performed using the Crank-Nicolson scheme:

$$\begin{aligned} \left(\rho u^n - \rho u^{n-1}, \varphi\right)_\Omega - \tfrac{1}{2}k_n\left(\rho v^n + \rho v^{n-1}, \varphi\right)_\Omega = 0, \\ \left(\rho v^n - \rho v^{n-1}, \psi\right)_\Omega + \tfrac{1}{2}k_n\left(a\nabla(u^n + u^{n-1}), \nabla\psi\right)_\Omega = 0, \end{aligned} \tag{5}$$

with u^0 and v^0 being the initial values. We chose this time stepping scheme because it is of second order and it is energy conserving, i.e.

$$\|\sqrt{\rho}v^n\|_\Omega^2 + \left\|\sqrt{a}\nabla u^n\right\|_\Omega^2 = \left\|\sqrt{\rho}v^{n-1}\right\|_\Omega^2 + \left\|\sqrt{a}\nabla u^{n-1}\right\|_\Omega^2.$$

This conservation property carries over to the the space-discretized equations provided that the meshes $\mathbb{T}^n$ do not change between time levels.

Since we use a primal formulation of the problem, the space discretization of (5) can be based on any one of the usual conforming Lagrangian finite element spaces $Q^r(\mathbb{T}^n)$ of degree r, which are defined on the computational grid $\mathbb{T}^n$ at time level t_n; these meshes may vary between the time levels in order to allow for grid refinement moving with the wave field. This

discretization leads to a system of two coupled matrix equations, which can be rewritten in decoupled form

$$\begin{aligned}\left(M + \tfrac{1}{4}k_n A\right) U^n &= \tilde{M}U^{n-1} + k_n\tilde{M}V^{n-1} - \tfrac{1}{4}k_n^2\tilde{A}U^{n-1},\\ MV^n &= \tilde{M}V^{n-1} - \tfrac{1}{2}k_n\left(AU^n + \tilde{A}U^{n-1}\right).\end{aligned} \tag{6}$$

Here, $M = (M_{ij})_{ij} = \left((\rho\varphi_i, \varphi_j)\right)_{ij}$ is the "mass matrix" and $A = (A_{ij})_{ij} = \left((a\nabla\varphi_i, \nabla\varphi_j)\right)_{ij}$ the "stiffness matrix" corresponding to the nodal basis functions $\varphi_i, \varphi_j \in Q^r(\mathbb{T}^n)$. $\tilde{M} = (\tilde{M}_{ij})_{ij} = \left((\rho\varphi_i, \tilde{\varphi}_j)\right)_{ij}$ and $\tilde{A} = (\tilde{A}_{ij})_{ij} = \left((a\nabla\varphi_i, \nabla\tilde{\varphi}_j)\right)_{ij}$ are matrices linking the finite elements functions $\varphi_i \in Q^r(\mathbb{T}^n)$ and $\tilde{\varphi}_j \in Q^r(\mathbb{T}^{n-1})$.

These two equations, a discrete Helmholtz equation and a discrete L^2-projection, are solved by a preconditioned conjugated gradient method; we use symmetric Gauss-Seidel or multigrid as preconditioner.

For the approach to error estimation which we will present in the next section, it is important to note that the above discretization in time and space can be interpreted as a simultaneous Galerkin discretization in space-time. By a straightforward calculation, we can formulate it is follows: Find $\mathbf{w}_h = \{u_h, v_h\} \in \mathcal{W}_h$, such that

$$a(\mathbf{w}_h, \boldsymbol{\tau}_h) = \left(\rho\mathbf{w}^0, \boldsymbol{\tau}_h(0)\right)_\Omega \qquad \forall\boldsymbol{\tau}_h = \{\varphi_h, \psi_h\} \in \mathcal{T}_h. \tag{7}$$

Functions in $\mathcal{W}_h$ and $\mathcal{T}_h$ are discrete functions of the time and space variables. We can recover the time discretization by the Crank-Nicolson scheme and the space discretization by finite elements by the following choice of function spaces:

$$\begin{aligned}\mathcal{W}_h = \big\{\mathbf{w}_h = \{u_h, v_h\} : \; & \mathbf{w}_h(\mathbf{x}, t) \text{ globally continuous},\\ & \mathbf{w}_h(\cdot, t)|_{I_n} \in \left(Q^r(\mathbb{T}^n) \cup Q^r(\mathbb{T}^{n-1})\right)^2,\\ & \mathbf{w}_h(\cdot, t_n) \in \left(Q^r(\mathbb{T}^n)\right)^2,\\ & \mathbf{w}_h(\mathbf{x}, t)|_{I_n} \text{ linear in } t\big\},\end{aligned} \tag{8}$$

$$\begin{aligned}\mathcal{T}_h = \big\{\boldsymbol{\tau}_h = \{\varphi_h, \psi_h\} : \; & \boldsymbol{\tau}_h(\cdot, t) \text{ continuous in } \Omega,\\ & \boldsymbol{\tau}_h(\mathbf{x}, t)|_{I_n} \text{ constant in } t,\\ & \boldsymbol{\tau}_h(\cdot, t)|_{I_n} \in \left(Q^r(\mathbb{T}^n)\right)^2\big\}.\end{aligned} \tag{9}$$

Note that in the construction of $\mathcal{W}_h$ we have associated the triangulations $\mathbb{T}^n$ with discrete time levels instead of the time slabs. In the interior of time slabs we let $\mathbf{w}_h$ be from the union of the finite element spaces defined on the triangulations at the two adjacent time levels. This construction is necessary to allow for trial functions that are continuous also at discrete time levels even if grids change between time steps. Associating triangulations with time slabs instead of time levels would yield a time stepping scheme which includes jump terms due to the discontinuity at discrete time levels. However, unlike for methods from the family of discontinuous-in-time Galerkin schemes (c.f. Johnson [17]) the two function values at a discontinuity are coupled and do not represent different degrees of freedom.

While we use hierarchically refined meshes, where the grids on the different time steps share a common coarse grid, the methods described in this paper are not restricted to these meshes. We note, however, that the transfer of solutions between different grids by projection is prohibitively expensive if general unstructured meshes are used.

For use in the next sections, we finally define a subdivision $S(\mathbb{T}^{n-1}, \mathbb{T}^n)$ of Ω, as follows:

$$S(\mathbb{T}^{n-1}, \mathbb{T}^n) := \left\{ \omega \subset \Omega \mid \exists K \in \mathbb{T}^{n-1}, K' \in \mathbb{T}^n : \omega = K \cap K' \right\}.$$

In two dimensions, this set is the subdivision of Ω by the union of mesh lines of $\mathbb{T}^{n-1}$ and $\mathbb{T}^n$. Due to the irregular structure of the elements of $S(\mathbb{T}^{n-1}, \mathbb{T}^n)$, computations are only feasible with reasonable effort if the grids $\mathbb{T}^{n-1}$ and $\mathbb{T}^n$ are related in some way. We note that for hierarchically refined grids, $S(\mathbb{T}^{n-1}, \mathbb{T}^n)$ is the set of most refined cells from the two grids.

3 Error estimation

3.1 Preliminary remarks

Before we start out with the derivation of a posteriori error estimates, we would like to clarify in what sense we will try to bound the error. Traditional *a priori* error analysis usually yields error bounds like

$$\begin{aligned} \|u(\cdot,T) - u_h(\cdot,T)\|_\Omega \leq C_1(T)\, k^2 \left\{ \sup_{0<t<T} \left\|\partial_t^3 u(\cdot,t)\right\|_\Omega + \sup_{0<t<T} \left\|\partial_t^2 \nabla u(\cdot,t)\right\|_\Omega \right\} + \\ + C_2(T)\, h^{r+1} \left\{ \sup_{0<t<T} \left\|\partial_t^2 \nabla^r u(\cdot,t)\right\|_\Omega + \sup_{0<t<T} \left\|\nabla^{r+1} u(\cdot,t)\right\|_\Omega \right\}, \quad (10) \end{aligned}$$

with h, k being the maximum space and time mesh size, respectively; see Hulbert and Hughes [16], Johnson [17], Bales and Lasiecka [1], and French and Peterson [12]. However, (10) is not what one is usually interested in in practical applications from science and engineering, for the following reasons:

- The constants C_i are unknown and estimates for them are usually too pessimistic.
- The exact solution u, which is unknown as well, enters the estimate.
- The required derivatives of the exact solution might not exist everywhere.
- The norm $\|u(\cdot,T) - u_h(\cdot,T)\|_\Omega$ might not be the quantity we want to control.

We will use *a posteriori* estimates to compensate for the unknown u and the problem of nonexistent derivatives. The last point is important in practical applications, since bounds on L_2 or energy norms often do not allow to also bound the error with respect to other quantities of interest. In particular, it should be noted that *a priori* estimates are almost exclusively available for global (in space or space-time) norm-like quantities, while from an application viewpoint localized quantities are of greater interest.

To illustrate our approach, let us assume our quantity of interest be a functional $J(\cdot)$ of the solution $\mathbf{w} = \{u, v\}$, which we will assume to be linear, for brevity. Examples for such functionals are

$$J(\mathbf{w}) = \partial_t u(\mathbf{x}_0, T), \qquad J(\mathbf{w}) = \int_C \mathbf{n}\cdot\nabla u(\mathbf{x}, T)\, ds,$$

$$J(\mathbf{w}) = \int_{\Omega_0 \subset \Omega} u(\mathbf{x}, T)\, dx, \qquad J(\mathbf{w}) = \int_0^T u(\mathbf{x}_0, t)\, dt,$$

denoting point evaluations, and integrals over curves C, subdomains Ω_0, or over time intervals. Nonlinear functionals can be used after linearization as well, see [2, 6], but we will not pursue this here. We will refer to $J(\cdot)$ by the names *target functional* or *error functional*.

Since the exact value $J(\mathbf{w})$ is the quantity to be computed to best accuracy, but only $J(\mathbf{w}_h)$ is available, it will be our aim in the next subsections to derive a posteriori estimates for the error

$$\mathcal{E} = J(\mathbf{w}) - J(\mathbf{w}_h). \tag{11}$$

Note that due to the assumed linearity of the target functional, $\mathcal{E} = J(\mathbf{e})$, with the error $\mathbf{e} = \mathbf{w} - \mathbf{w}_h$. The practical derivation of estimates for $\mathcal{E}$ uses a method proposed in [7] which is based on the general concept of residual-based a posteriori error estimation introduced in Eriksson and Johnson [11] and Eriksson, et al. [10]; see also Johnson [17] for the application of this approach for the wave equation.

3.2 Derivation of an error estimator

In order to derive an exact representation formula for the error, we first note that due to (2) and its discrete form (7), the error $\mathbf{e} = \mathbf{w} - \mathbf{w}_h$ satisfies an orthogonality relation with respect to the bilinear form $a(\cdot,\cdot)$:

$$a(\mathbf{e}, \boldsymbol{\tau}_h) = 0, \quad \boldsymbol{\tau}_h \in \mathcal{T}_h. \tag{12}$$

This property of finite element methods is called "Galerkin orthogonality".

For deriving our error estimate, we employ a duality argument as used by Johnson [17] for analyzing the *discontinuous* Galerkin approximation of the wave equation. We first define a continuous dual problem: Find $\mathbf{w}^* = \{u^*, v^*\} \in W^*$, such that

$$a^*(\mathbf{w}^*, \boldsymbol{\tau}) = J(\boldsymbol{\tau}) \qquad \forall \boldsymbol{\tau} \in T^*, \tag{13}$$

with the dual bilinear form

$$a^*(\mathbf{w}^*, \boldsymbol{\tau}) = -(\rho\partial_t \mathbf{w}^*, \boldsymbol{\tau})_{Q_T} + \left(\begin{pmatrix} 1 & 0 \\ 0 & \nabla \end{pmatrix} \mathbf{w}^*, \begin{pmatrix} 0 & -\rho \\ a\nabla & 0 \end{pmatrix} \boldsymbol{\tau} \right)_{Q_T} + (\rho \mathbf{w}^*(T), \boldsymbol{\tau}(T))_\Omega,$$

which resembles a wave equation for v^*,

$$\rho\partial_t^2 v^* - \nabla\cdot a\nabla v^* = j_1 - \partial_t j_2,$$

with $u^* = -\partial_t v^* - \rho^{-1}\partial_t j_2$, and the functions $\mathbf{j}(\mathbf{x}, t) = \{j_1, j_2\}$ defined by $J(\boldsymbol{\tau}) = (\mathbf{j}, \boldsymbol{\tau})_{Q_T}$. Note that the integral kernels $\mathbf{j}$ may be Dirac functions if the integration in $J(\cdot)$ extends over a manifold of dimension less than $d+1$. Final values $\mathbf{w}^*(T)$ are therefore also provided by $\mathbf{j}$.

Here, $W^* = H^1(I, L_2(\Omega)) \times H^1(I, H^1(\Omega))$, and T^* is a subset of $L_2(I, H^1(\Omega)) \times L_2(I, L_2(\Omega))$ consisting of functions left-continuous in time. Since $W \subset T^*$, note that if $\boldsymbol{\tau} \in W$, we get $a^*(\mathbf{w}^*, \boldsymbol{\tau}) = a(\boldsymbol{\tau}, \mathbf{w}^*)$ by partial integration with respect to the time variable. If we therefore test with $\boldsymbol{\tau} = \mathbf{e} \in W$ and use Galerkin orthogonality, we obtain

$$\mathcal{E} = J(\mathbf{e}) = a(\mathbf{e}, \mathbf{w}^* - \mathbf{w}_h^*) \tag{14}$$

for any $\mathbf{w}_h^* \in \mathcal{T}_h$. Recalling the definition of the bilinear form $a(\cdot,\cdot)$ and integrating by parts on each sub-cell $K \in S(\mathbb{T}^{n-1}, \mathbb{T}^n)$, we obtain the following result.

Proposition 1 *For the Galerkin finite element approximation* (7) *of the wave equation* (1) *there holds the error identity*

$$\mathcal{E} = \sum_{K\in\mathbb{T}^0} \mathcal{E}_{K,0} + \sum_{n=1}^{N} \left[\sum_{K\in S(\mathbb{T}^{n-1},\mathbb{T}^n)} \mathcal{E}_{K,n} \right], \tag{15}$$

with the cell-wise error indicators

$$\begin{aligned} \mathcal{E}_{K,n} &= -\left(r_1, u^* - u_h^*\right)_{K\times I_n} - \left(r_2, v^* - v_h^*\right)_{K\times I_n} - \tfrac{1}{2}\left(\mathbf{n}\cdot\mathbf{r}_{\partial K}, v^* - v_h^*\right)_{\partial K\times I_n}, \\ \mathcal{E}_{K,0} &= \left(\rho(\mathbf{w}^0 - \mathbf{w}_h(0)), \mathbf{w}^*(0) - \mathbf{w}_h^*(0)\right)_K, \end{aligned} \tag{16}$$

where $\mathbf{w}_h^* = \{u_h^*, v_h^*\} \in \mathcal{T}_h^*$ *is arbitrary, and*

$$r_1 = \rho u_{h,t} - \rho v_h, \qquad r_2 = \rho v_{h,t} - \nabla\cdot a\nabla u_h, \qquad \mathbf{n}\cdot\mathbf{r}_{\partial K} = \mathbf{n}\cdot[a\nabla u_h]$$

denote the cell residuals of the two equations and the jump of the conormal derivative of u_h *between two adjacent cells, respectively; these residuals are computable.*

Remark: In order to retain the optimal order of convergence not only globally, but also locally, one has to use the liberty to choose $\mathbf{w}_h^*$. Since r_2 does not converge to zero, we take $\mathbf{w}_h^*$ to be a suitable interpolation of $\mathbf{w}^*$ with local projection properties (see [6] for an example of such a construction); one can then replace

$$\left(r_2, v^* - v_h^*\right)_{K\times I_n} = \left(r_2 - \bar{r}_2, v^* - v_h^*\right)_{K\times I_n},$$

with $\bar{r}_2$ being the projection of r_2 into the corresponding polynom space.

Eq. (15) makes reference to the unknown continuous dual solution $\mathbf{w}^*$. Hence, in evaluating it, we have to replace $\mathbf{w}^*$ by a suitable numerical approximation. For this, there are several possible methods, see [6]. Commonly, one of the following two ways is chosen:

- Directly replace $\mathbf{w}^*$ in (16) by a numerical approximation $\widetilde{\mathbf{w}}^*$. When using this approach, care must be taken to choose $\widetilde{\mathbf{w}}^*$ sufficiently far away from $\mathcal{T}_h$ since otherwise we could choose $\mathbf{w}_h^* \in \mathcal{T}_h$, such that we essentially cancel out $\widetilde{\mathbf{w}}^*$. Two common approaches to this problem are to either compute the numerical dual solution $\widetilde{\mathbf{w}}^*$ by a higher order method, for example with finite elements of degree $r+1$, or to compute a $\overline{\mathbf{w}}^*$ with the same method and set $\widetilde{\mathbf{w}}^* = I_h^{r+1}\overline{\mathbf{w}}^*$ to be the patchwise interpolation of degree $r+1$. Due to the complications inherent to the practical computation of the special $\mathbf{w}_h^*$ noted above, we do not use it in our code but set $\mathbf{w}_h^* = I_h\widetilde{\mathbf{w}}^*$, i.e. the nodal interpolation in $\mathcal{T}_h$. Accordingly we do not subtract $\bar{r}_2$ also.

  In principle, it is also necessary to use higher order approximations in time, either for direct approximation of $\mathbf{w}^*$ or as the result of an extrapolation process. However, both possibilities are prohibitively more expensive than using higher order approximations in space only, since the data of more than two time steps, possibly defined on different grids each, has to be accessed. Therefore, in the computations presented below we have chosen the cheaper option.

- Using the Cauchy-Schwarz inequality yields

$$|\mathcal{E}_{K,n}| \le \|r_1\|_{K\times I_n}\|u^* - u_h^*\|_{K\times I_n} + \|r_2 - \bar{r}_2\|_{K\times I_n}\|v^* - v_h^*\|_{K\times I_n} + \tfrac{1}{2}\|\mathbf{n}\cdot r_2\|_{\partial K\times I_n}\|v^* - v_h^*\|_{\partial K\times I_n}, \tag{17}$$

  and similar estimates for $\mathcal{E}_{K,0}$. One can then use a variant of the Bramble-Hilbert lemma for polynomials of different degree in space and time directions, to estimate

$$\|u^* - u_h^*\|_{K\times I_n} \le C\left(h_K^{r+1}\|\nabla^{r+1}u^*\|_{\tilde{K}\times I_n} + k_n\|\partial_t u^*\|_{\tilde{K}\times I_n} + k_n^{r+1}\|\partial_t^{r+1}u^*\|_{\tilde{K}\times I_n}\right),$$

  with a patch of cells $\tilde{K}$ suitably chosen around K.

  We can now approximate $\mathbf{w}^*$ by a numerical solution $\widetilde{\mathbf{w}}^* = \{\tilde{u}^*, \tilde{v}^*\}$ which we can compute with the same polynomial degree r as for the primal solution $\mathbf{w}_h$; in this case, the derivatives ∇^{r+1} and ∂_t have to be replaced by suitable difference quotients $\nabla_h\nabla^r$ and $\partial_{t,h}$. In view of the inverse property of finite elements, we assume that we can replace $\|\partial_t^{r+1}u^*\|_{K\times I_n} \to k_n^{-r}\|\partial_t u_h^*\|_{K\times I_n}$, to obtain

$$\|u^* - u_h^*\|_{K\times I_n} \le C\left(h_K^{r+1}\|\nabla_h\nabla^r\tilde{u}^*\|_{K\times I_n} + k_n\|\partial_{t,h}\tilde{u}^*\|_{K\times I_n}\right) \tag{18}$$

  for the first term in (17). The other two terms in (17) can be estimated in a similar way. For the last one, a trace inequality has to be applied first.

The second way obviously is numerically less expensive since neither higher order finite element solutions nor patchwise interpolations have to be computed. However, the loss of the sign of $\mathcal{E}_{K,n}$ makes its results questionable. This can easily be demonstrated by the following example: assume exact and numerical solution as well as the computational grids are symmetric with respect to the origin and the target functional is an antisymmetric evaluation of its argument, e.g. $J(\mathbf{w}) = K(\mathbf{w}(\mathbf{x},t)) - K(\mathbf{w}(-\mathbf{x},t))$ with an arbitrary functional K. Then the exact error $J(\mathbf{e}) \equiv 0$ due to cancellation of error contributions of pairs of space-time cells with locations symmetric with respect to the origin. However, after using the Cauchy-Schwarz inequality, the computed estimate $\sum|\mathcal{E}_{K,n}|$ to the exact error will be different from zero.

We should remark that although the given example for $J(\cdot)$ is academic, cancellation of contributions of space-time cells $K\times I_n$ to $\mathcal{E}$ plays an important role if the region of evaluation of $J(\cdot)$ extends over more than one wave length in space, or over more than one period in time. These considerations show that the proposed second way, though successfully used for several equations such as Laplace's equation [6], the heat equation (Hartmann [14]), radiative transfer (Kanschat [18]) or in elasto-plasticity [23], poses problems in case of equations with oscillatory solutions.

For the present work, we therefore choose the first approach. We use higher order approximations instead of patchwise interpolations in space, which choice is motivated by academic reasons, however, and is obviously not the way to go if computational resources are limited. As time stepping scheme for the approximation $\widetilde{\mathbf{w}}^*$ to $\mathbf{w}^*$ we use the Crank-Nicolson scheme as well, lacking practical alternatives of higher order. Since the solutions produced by this method are piecewise linear and continuous in time, but the elements of $\mathcal{T}_h$ are piecewise constant and discontinuous, the term $\widetilde{\mathbf{w}}^* - \mathbf{w}_h^*$, with $\mathbf{w}_h^*$ chosen as the interpolation of $\widetilde{\mathbf{w}}^*$ at the midpoint of each time interval, does indeed contain some information in time; however, it is questionable whether the distance of the solutions with respect to $\mathcal{T}_h$ is large enough in this case to fully justify the replacement $\mathbf{w}^* \to \widetilde{\mathbf{w}}^*$. Better alternatives will have to be employed here in the future.

3.3 A global-norm error indicator

Sometimes, the target functional one is interested in is sufficiently global such that its domain of influence (which is given by the support of the dual solution) is more or less the whole domain. Then one does not gain much by solving for the dual solution and one can get cheaper error indicators than the one above by using analytical a priori estimates for the dual solution. We refer to Johnson [17] for corresponding analysis of the discretization of the wave equation by the *discontinuous*-in-time Galerkin finite element method.

The derivation of error estimates in global norms using a priori estimates for the dual solution is well known for Laplace's equation. We would like to compare the grids obtained by the weighted error estimator derived in the previous section with those resulting from the use of one of these "traditional" error indicators. Without further justification, we select the one proposed by Kelly, et al. [19]:

$$\eta_{K,n} = h_K^{1/2} \|\mathbf{n}\cdot\mathbf{r}_{\partial K}\|_{\partial K \times I_n}. \tag{19}$$

Since we only refine the spatial grid, we have neglected the time step size k_n. We will refer to (19) by the name "energy error indicator", since it was originally derived as an indicator for the energy norm of the error.

Apart from its usefulness for Laplace's equation, (19) can be made plausible by observing that for finite elements of odd polynomial degree, the cell terms in (16) are of higher order in the mesh width than the jump terms and therefore may be neglected. However, a rigorous derivation of (19) is missing for the formulation and discretization of the wave equation used in this paper.

4 Numerical results

In this section, we show some numerical examples which illustrate the error estimation approach derived above. The computations were performed with a program based on the `deal.II` library described in [4, 3]. It allows the simulation of acoustic waves in one, two, and three spatial dimensions. We chose a set of examples to demonstrate the following features of our approach:

- By *Example 1*, an example of wave propagation in one spatial dimension, we try to illustrate the way by which our approach works and how the resulting grids depend on the primal solution and the solution of the dual problem derived from the target functional.
- By *Example 2*, we investigate how the grid refinement procedure reacts to numerical disturbances. For this, we choose the well-known effect of spurious reflections at discontinuities of the mesh size which is commonly viewed as one of the main obstacles for adaptive methods for the computation of wave propagation.
- In *Example 3*, we present numerical results for an example, again in one space dimension, involving more complex propagation of waves due to a discontinuous elasticity coefficient a. This includes a comparison of the number of space-time cells needed by the different methods of grid refinement presented in the last section, to obtain a given accuracy. It also shows the efficiency in estimating the actual error with respect to the target functional.

- In the final *Example 4*, we present a non-trivial case of two dimensional wave propagation.

In all examples, we set the density parameter ρ equal to one.

Example 1: One dimensional wave propagation. Consider eq. (1) for $d = 1$, $\rho = a = 1$, and $\Omega = (-1, 1)$. We choose initial and boundary conditions as shown in Figure 1. The half width is chosen to be $s = 0.1$ and the end time as $T = 2.7$. Computations in this and the following examples are performed with linear elements in space and the time discretization as described in Section 2.

$$
\begin{aligned}
u^0(x) &= \exp\left(-\frac{x^2}{s^2}\right)\left(1 - \frac{x^2}{s^2}\right)\theta\left(1 - \frac{|x|}{s}\right), \\
v^0(x) &= 0, \\
\partial_x u(-1) &= 0, \\
\partial_x u(1) &= 0,
\end{aligned}
$$

with the jump function

$$
\theta(y) = \begin{cases} 0 & \text{for } y < 0, \\ 1 & \text{for } y \geq 0. \end{cases}
$$

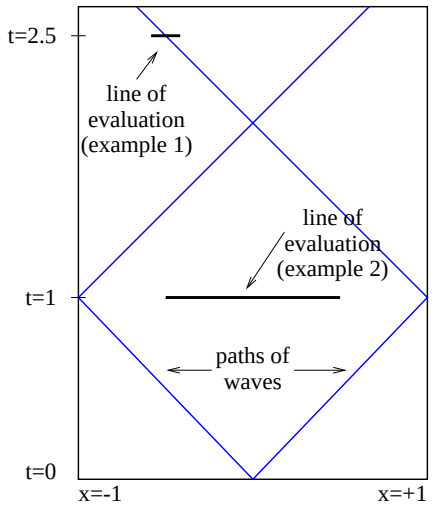

Figure 1: *Configuration of Examples 1 and 2.*

We are now interested in the evaluation of only one branch of the solution, for example the one initially traveling to the right. This is a rather frequent case if one wants to compare the outcome of a simulation with measurements. Here we choose to localize the measurements at $t = 2.5$ and around $x = -0.5$ and use as target functional the quantity

$$
J(\boldsymbol{\tau}) = \int_{-0.6}^{-0.4} \varphi(x, 2.5)dx,
$$

with $\boldsymbol{\tau} = \{\varphi, \psi\}$. Note that the solution's two peaks are centered around $x = \pm 0.5$ at $t = 2.5$, with diameter 0.2 as in the initial distribution. The solution u^* of the corresponding dual problem is shown in Fig. 2 on the left. As can easily be seen, the integral kernel of the functional $J(\cdot)$, i.e. the characteristic function of $[-0.6, 0.4] \times \{2.5\}$, serves as source term for the dual solution. The true dual solution therefore is discontinuous due to the discontinuous integral kernel.

By (15), we now compute error estimates and refine the grid accordingly. The resulting space-time grid after three refinement cycles is shown in Fig. 2. As can be seen, the error estimator does not only do the obvious thing, which would be to track just one branch of the two waves, but does also take into account errors occuring in the whole space-time domain. It is therefore far better than a priori refining the mesh by hand, because one would not refine the other branch at all. On the other hand, the branch leading directly to the region

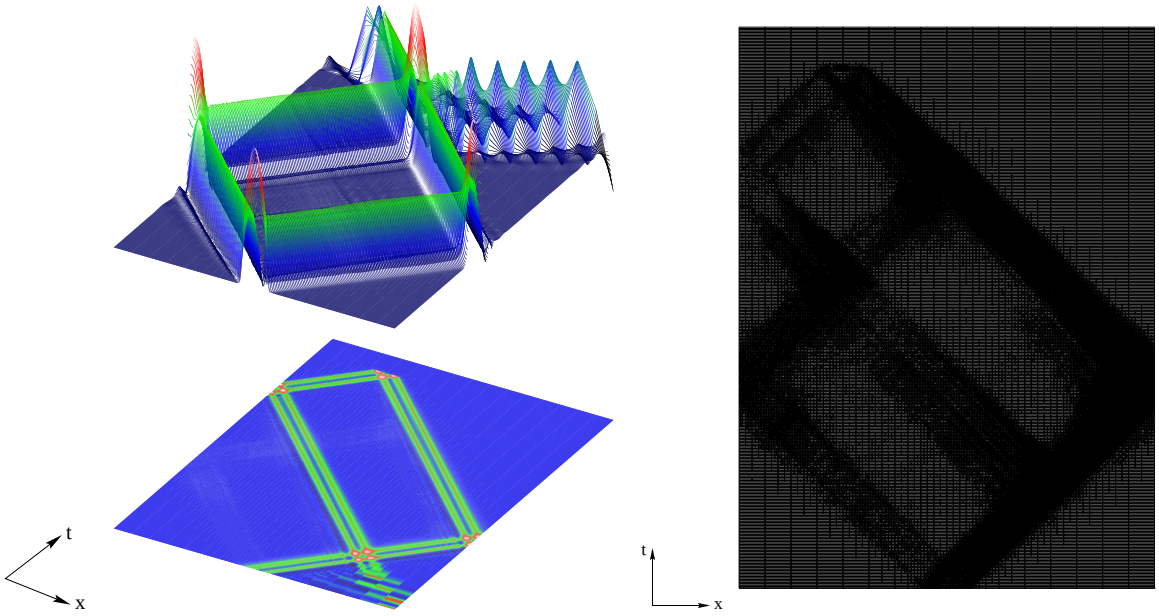

Figure 2: *Example 1. Left: primal solution u and dual solution u^*. (Note that the dual solution is solved backward in time.) Right: resulting space-time grid after three cycles of refinement.*

of evaluation is much more refined, due to the larger weighting in (15). Also note the very coarse grid for $t > 2.5$; it is coarsened in each refinement cycle and will end up in only one cell on each time level after some cycles. This is the reason for the bad resolution of the solution at late times. Since the one-dimensional case with constant coefficients is too easily solved to four or five digits of accuracy, we do not show convergence charts in this and the following example.

Example 2. By this example, we want to demonstrate two aspects of the mechanism by which the error estimator refines a grid. We consider the same setting as in Example 1, but with the modified target functional

$$J(\boldsymbol{\tau}) = \int_{-0.5}^{+0.5} \varphi(x,1)\, dx,$$

with $\boldsymbol{\tau} = \{\varphi, \psi\}$. It is obvious from Fig. 1 that the exact value of the functional is $J(\mathbf{w}) = 0$.

We now choose the grid such that it is fine enough in the region $x > -\frac{1}{3}$ ($h = \frac{1}{48}$) and too coarse to resolve the solution for $x < -\frac{1}{3}$ ($h = \frac{1}{6}$). In Fig. 3 the primal solution u is shown along with the space-time grid. It is a well-known phenomenon that waves are partially reflected from discontinuities of the mesh-size (see, e.g., Bažant [5], and Harari [13]), which can also be seen in this example. In general, we have to expect our error estimator to produce such sharp transitions in the mesh size at places where waves leave the domain of influence of the target functional. In the first example this applies to the branch of the wave which does not enter the evaluation of $J(\cdot)$ and which is not well resolved at all after about $t = 2$ when the two branches meet for the last time. The question now is: will the target functional be

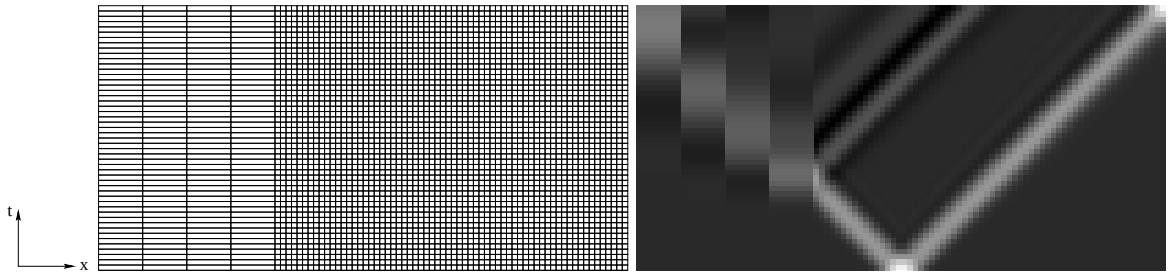

Figure 3: *Example 2. Left: Initial space-time grid. Right: primal solution* u *.*

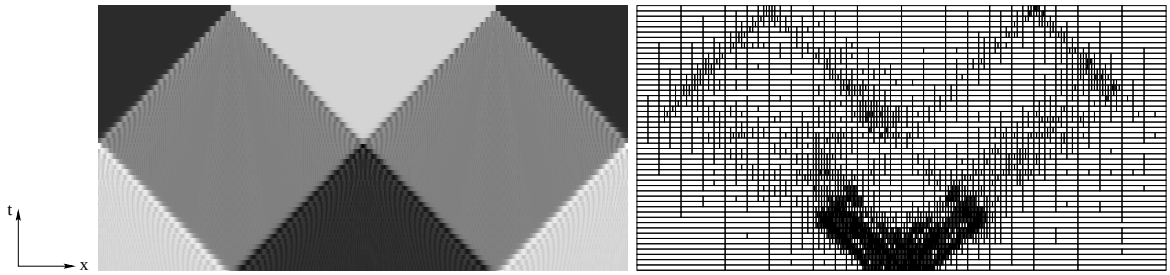

Figure 4: *Example 2. Left: dual solution* u^* *. Right: grid after four cycles of refinement.*

affected by the reflections produced when this second branch runs into a region with a coarse grid?

In the present case the reflections from the grid discontinuity affect the evaluation of the target functional and we hope that the dual estimator will "see" this. To investigate this question, we show the dual solution u^* in Fig. 4 and the error distribution on the first grid in Fig. 5. As we expected, the cell indicators $\mathcal{E}_{K,n}$ are large in the region where the grid is coarse. However, we should remark that this is the region where the error (with respect to the target functional) is produced and that the error values are small along the path of the spurious waves traveling into the region of evaluation of $J(\cdot)$ at the end time. The error estimator is therefore able to separate between the regions where the error $\mathbf{e} = \mathbf{w} - \mathbf{w}_h$ is *generated* and where it is only *propagated*. The grid after four cycles of refinement is also shown in Fig. 4; the discontinuity in the initial mesh size is no more visible.

The grid in Fig. 4 also shows that the refinement is directed mostly towards the edges of the domain of evaluation, instead of the whole interior. The reason for this behavior is connected to the special structure of the dual solution (see Fig. 4). The exact dual solution u^* is piecewise constant in the interior of the different regions and therefore the weights $u^* - u_h^*$ in the error representation (15) are zero. The terms involving u^* therefore only contribute at the boundaries of these regions. This corresponds to the fact that large residuals mean spurious oscillations. These, however, do not affect the mean value of u as in the evaluation of $J(\cdot)$, unless the integration extends over less than the whole oscillation. The latter happens only at the boundaries of the domain of influence, which are also the boundaries between the different regions, i.e. where u^* is discontinuous.

In contrast to this, v^* is piecewise constant in space but piecewise linear in time, and therefore $v^* - v_h^* \neq 0$ in the interior of the different regions since v_h^* is only piecewise constant

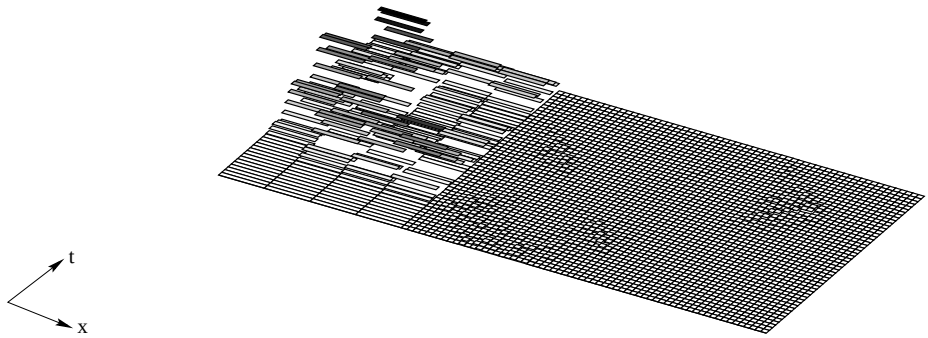

Figure 5: *Example 2. Distribution of* $|\mathcal{E}_{K,n}|$ *on the first grid.*

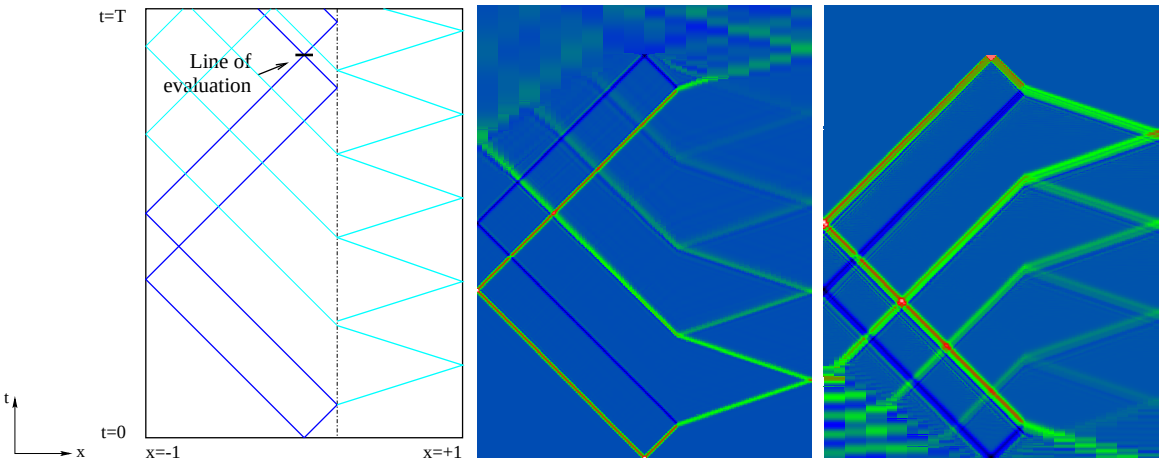

Figure 6: *Example 3. Left: layout of the space-time domain; the position of the discontinuity of the coefficient as well as the most important waves are plotted. Middle: primal solution* u *. Right: dual solution* u^* *. The solutions are plotted after three cycles of refinement of the space-time initial mesh.*

in time. Thus, some grid refinement will occur also inside these regions.

Example 3. One dimensional wave propagation with high frequency and discontinuous coefficients. As a more challenging problem, we take a similar situation as in the previous example. In particular, we use the same initial values, but this time with a frequency ten times as high, $s = 0.01$. In addition, we choose a discontinuous elasticity coefficient, $a = 1$, for $x < 0.2$ and $a = 9$ for $x \geq 0.2$. The wave velocity to the right of the discontinuity is therefore three times as high as to the left. The layout of the problem as well as a numerical solution are shown in Fig. 6.

As target functional, we choose

$$J(\boldsymbol{\tau}) = \int_{-0.03}^{0.03} \varphi(x, 2.4)\ dx,$$

with $\boldsymbol{\tau} = \{\varphi, \psi\}$. As indicated in Fig. 6, this is the place where the two waves traveling to the

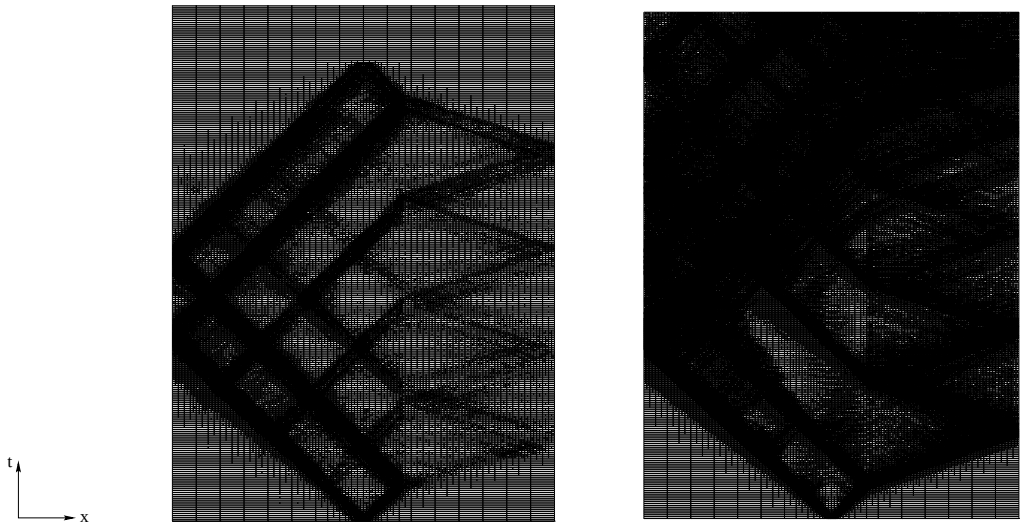

Figure 7: *Example 3. Space-time grids produced by the dual estimator* (15) *and by the simplified energy estimator* (19)*, after three cycles of refinement.*

left and the right meet again after one reflection from the discontinuity. In addition, another wave traveling back and forth between right boundary and discontinuity travels nearby as well. The dual solution corresponding to this target functional is also shown in Fig. 6.

In order to evaluate the method under consideration, we compare the results of computations performed on grids refined by the dual estimator (15), by the energy error indicator (19), and by global refinement. The time step is chosen to be $k = 0.0008$ which equals a ratio of 50 time steps per period for the lowest frequency in the region with $a = 1$ (there, the natural time scale is $\tau = 4s$), and roughly 16 time steps per period in the region with $a = 9$ ($\tau = 4s/\sqrt{a}$). However, higher frequencies are significant in this example as well. We note that the cells of the spatial mesh have an initial size of $1/32$. Therefore, in the region with $a = 1$ the CFL number $(k_n\sqrt{a})/(h_K\sqrt{\rho})$ becomes larger than one for the most refined cells in the sixth refinement step, and in the fourth step in the region with $a = 9$.

In Fig. 7 grids for the two types of error indicators are shown. It is clearly seen that the grids resulting from (19) are denser and, as must be expected, are not adapted to the target functional. In Fig. 8 we compare the convergence of the target functional for the different methods of refinement. As can be seen, the dual estimator is able to produce a computational grid which is *significantly* more economical than the one produced by the energy indicator and the globally refine grid.

The relatively small errors for global refinement as compared to the energy error indicator (19), in particular the first value, can be attributed to the fact that the time stepping scheme used in this study is known to produce oscillations in front and behind the main wave, which are much stronger on globally refined grids than on locally refined ones. However, they do not affect much the mean value computed in $J(\mathbf{w}_h)$, which is why their error measured with respect to the target functional is smaller than for refinement by (19); when measured in a global norm, the solutions obtained on globally refined grids are much less accurate. With regard to the first data point, the fringe waves mentioned above are too far away from the main wave due to the coarse grid, so they do not affect the evaluation of $J(\mathbf{w}_h)$ much, which

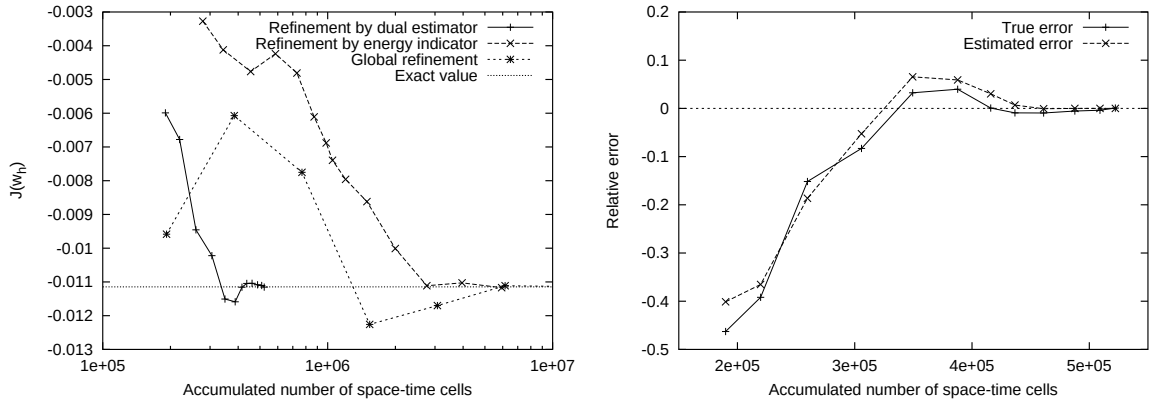

Figure 8: *Example 3. Left: values of the target functional* $J(\mathbf{w})$ *for refinement by the dual estimator* (15)*, by the simplified energy error indicator* (19)*, and by global refinement. Right: true error* $J(\mathbf{e})$ *and estimated error* $\tilde{\mathcal{E}}$*, for refinement by the dual error estimator.*

is localized around the main wave.

While (15) yields a good refinement criterion as shown above, it was derived as an error estimator. It is therefore interesting to see whether we can also get accurate estimates for the error from it. Table 1 shows the computed values $J(\mathbf{w}_h)$ and their deviation from the true value $J(\mathbf{w})$ which is

$$J(\mathbf{w}) = \frac{s}{2}\sqrt{\pi}\,\mathrm{erf}(1) + \frac{s}{e} \approx 0.011147.$$

In Fig. 8 and Table 1, the true error, $J(\mathbf{e}) = J(\mathbf{w}) - J(\mathbf{w}_h)$, is now compared against the estimated error as obtained from (15) evaluated with a numerically obtained dual solution of one polynomial degree higher than the primal one. We will denote the evaluated error identity by $\tilde{\mathcal{E}}$; N denotes the number of space-time cells accumulated over all time steps in the time interval $[0, 2.4]$. Up until the fifth iteration, the error reduces monotonically. However, since we do not refine the time discretization in this example, the CFL number is getting significantly larger than one, at which point the non-decreasing time discretization error starts to dominate the total error. The reduction of error then stalls and shows a somewhat erratic behavior at this low level. At this point also the error estimates become rather unreliable, which we attribute to the problems mentioned at the end of Section 3, namely the computation of the numerical dual solution by the same time stepping scheme. This is suggested by the fact that the error estimates tend to zero while the true error does not.

It should be noted, however, that while the relative error is in the range of more than one per cent, the error estimate is quite reliable and follows the true error within a reasonable distance. In particular note that it predicts the sign of the error correctly in this range.

With the present example we would also like to investigate another aspect of our approach. In order to evaluate (15) numerically several possibilities were sketched in Section 3. We here compare the following methods:

- *Method 1:* Replace $\mathbf{w}^*$ by a numerically obtained solution $\widetilde{\mathbf{w}}^*$ which was computed

	N	$J(\mathbf{w}_h)$	$J(\mathbf{e})$	$\tilde{\mathcal{E}}$	$\tilde{\mathcal{E}}/J(\mathbf{e})$
1	189908	-0.00598	-0.00515	-0.00447	0.87
2	219755	-0.00677	-0.00436	-0.00407	0.93
3	259657	-0.00945	-0.00169	-0.00207	1.23
4	305734	-0.01022	-0.00092	-0.00058	0.63
5	349411	-0.01150	0.00036	0.00072	2.02
6	387773	-0.01158	0.00044	0.00065	1.49
7	415938	-0.01115	0.00001	0.00034	41
8	436568	-0.01104	-0.00010	0.00008	-0.75

Table 1: *Example 3. Comparison between true and estimated error. N denotes the number of space-time cells accumulated over all time steps. The erratic behavior from the sixth step onwards is explained in the text.*

with a polynomial degree one higher than that of the primal solution. As noted above, the polynomial degree in the time direction is not changed.

- *Method 2:* Replace $\mathbf{w}^*$ by a numerically obtained solution $\widetilde{\mathbf{w}}^*$ which was computed *with the same polynomial degree* as the primal solution. Again, in time we use the same approximation. We chose $\mathbf{w}_h^*$ as the natural nodal interpolation of $\widetilde{\mathbf{w}}^*$ in $\mathcal{T}_h$.

- *Method 3:* Apply the simplified error indicator (19), but weigh the value on each cell with $h_K^{-3}\|\mathbf{w}^* - \mathbf{w}_h^*\|_K \approx h_K^{-1}\left\|\nabla^2 \mathbf{w}^*\right\|_K \approx h_K^{-3/2}\|[\partial_n \tilde{v}^*]\|_{\partial K}$. Note that we have assumed $r = 1$ here and that we have neglected the time step, since that is taken constant throughout the computations in this paper; $\widetilde{\mathbf{w}}^*$ is computed using the same polynomial degree as for the primal solution.

While all the examples in this paper where computed with Method 1, except if noted otherwise, Method 2 would seem to not work at first glance. The reason is that by introduction of the element $\mathbf{w}_h^*$ due to Galerkin orthogonality, we can essentially cancel the difference $\widetilde{\mathbf{w}}^* - \mathbf{w}_h^*$ since both parts are piecewise polynomial with the same degree. However, because $\widetilde{\mathbf{w}}^* \in \mathcal{W}_h$ is piecewise linear in time, but $\mathbf{w}_h^* \in \mathcal{T}_h$ is piecewise constant, the difference does not exactly cancel out, but rather is a measure for the size of the time derivative. Due to the fact that for solutions of the wave equation space and time derivatives are somewhat coupled (see, e.g., eq. (4)), $\|\mathbf{w}^* - \mathbf{w}_h^*\|_{K\times I_n} \approx C(h, h/k, r)\|\widetilde{\mathbf{w}}^* - \mathbf{w}_h^*\|_{K\times I_n}$. It is obvious that $C(h, h/k, r) \to 1$ if $h \to 0$ and $h/k \to 0$.

In the examples presented in this work we do not change the time discretization but only refine the spatial mesh. Therefore, it is not surprising that Method 2 yields meshes which are almost as efficient as the ones generated by the more expensive first method. There is also no large visible difference between the meshes. However, we cannot expect the resulting estimates for the error to be good. Additionally, one has to start on a spatially finer mesh than with Method 1, in order to guarantee convergence of the meshes.

Contrary to Method 2, Method 3 does not take into account the time discretization error but only measures spatial smoothness of primal and dual solutions. We expect this method to yield good results on coarse grids but to return worse results if the spatial mesh is very fine. However, as with Method 2 we have to start on a grid once more refined than for Method 1

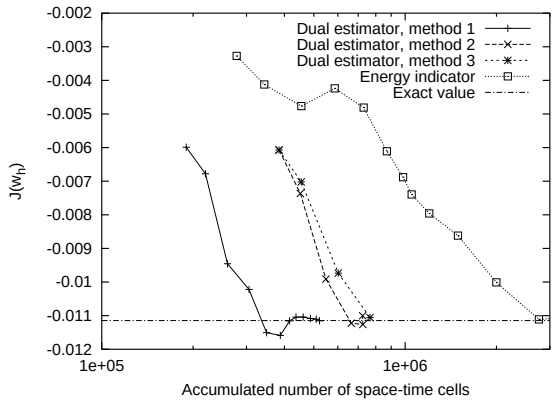

Figure 9: *Example 3. Convergence results for the different methods of evaluating the error identity. The results for refinement by the simplified energy error indicator are also shown for comparison.*

to ensure reasonable results. Methods 2 and 3 need to spend significantly less effort on the computation of the dual solution than Method 1.

The convergence histories for the different methods are shown in Fig. 9. It is seen that Method 2 converges equally fast to the exact value of $J(\cdot)$, but starting with a once more refined grid as noted above. Method 3 produces very similar grids as the first method, as well.

Example 4. Two-dimensional wave propagation. In this example we consider a situation similar to the previous one. Let $\Omega = (-1,1)^2 \subset \mathbb{R}^2$, and the initial values be

$$u^0(\mathbf{x}) = \exp\left(-\frac{\mathbf{x}^2}{s^2}\right)\left(1-\frac{\mathbf{x}^2}{s^2}\right)\theta\left(1-\frac{|\mathbf{x}|}{s}\right), \qquad v^0 = 0,$$

with the jump function θ as in the first example, and $s = 0.01$. Again, we choose the elasticity coefficient discontinuous, $a = 1$ for $y < 0.2$, and $a = 9$ for $y \geq 0.2$. A typical wave pattern is shown in Fig. 10.

In geophysics and seismics it is an important task to accurately model the signal arrival time at a given point. This situation often arises when comparing computed results with measured ones in inverse media problems, where we want to deduce the coefficient function $a(\mathbf{x})$ from measurements. In our case, we are interested in the situation at the point $\mathbf{x}_0 = (0.75, 0)$. As shown in the layout (see Fig. 10) the three first waves arriving at this point are the Huyghens' wave, the direct wave, and the one reflected from the discontinuity. Speaking in ray theoretical terms, the first one travels into the medium of higher wave velocity, travels some distance parallel to the discontinuity and then back towards the point of measurement. Among all waves it is the one which has the least action along its path and is therefore called Huyghens' wave. From extrapolation of computed data, we estimate its arrival time to be approximately $\tau_H \approx 0.618$ while the arrival times of the other ones are $\tau_d \approx \frac{3}{4} = 0.75$ for the direct wave and $\tau_r \approx \frac{17}{20} = 0.85$ for the reflected wave. The latter two values neglect the

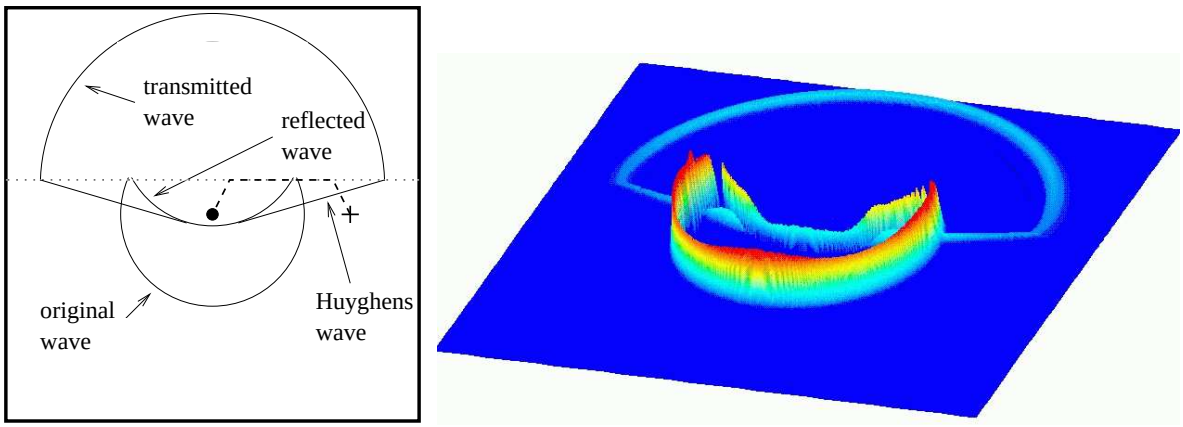

Figure 10: *Example 4. Left: layout of the wave pattern after some time; a bullet and a cross indicate the positions of source and receiver, respectively. The dotted line indicates the discontinuity in the coefficient, while the thick dashed line denotes the path of least action. Right: plot of the solution at* $t = 0.45$.

extension of the initial distribution u^0 . As arrival time we define

$$\tau = \frac{\int_{t_1}^{t_2} tu(\mathbf{x}_0, t)\ dt}{\int_{t_1}^{t_2} u(\mathbf{x}_0, t)\ dt}, \tag{20}$$

with a time interval (t_1, t_2) suitably chosen around the signal and such that it does not include other signals. This interval is usually chosen in accordance with experimental data. We take $t_1 = 0.55$ and $t_2 = 0.68$, to catch the first wave only. Accordingly we choose $T = t_2$ to stop the computation at the first possible time.

The proper target functional for this example would be a linearized form of the nonlinear functional (20). However, we note that the denominator in (20) is a mean value and therefore usually much better approximated than the numerator. It is therefore mostly a constant factor scaling the dual solution and if we sacrifice the goal of quantitative error control in this example, we may choose

$$J(\boldsymbol{\tau}) = \int_{t_1}^{t_2} t\varphi(x_0, t)\ dt,$$

with $\boldsymbol{\tau} = \{\varphi, \psi\}$.

In Fig. 11 we show the computational grids at times $t = 0.15$, $t = 0.45$ and $t = T$, as generated by refinement by the energy error indicator (19) and by the dual estimator (15). It is readily seen that the latter only tracks that part of the wave field that travels to the right. A closer look at a more complete sequence of grids than shown here reveals that the most refined parts of the grids indeed track the path of least action (the dashed line in Fig. 10) which marks the path of the first signal to arrive at the receiver. The first grid shown is at a time where the wave to arrive first is still traveling upward, while in the second it is already traveling downward again. These complicated features of wave propagation are clearly reflected in the grids.

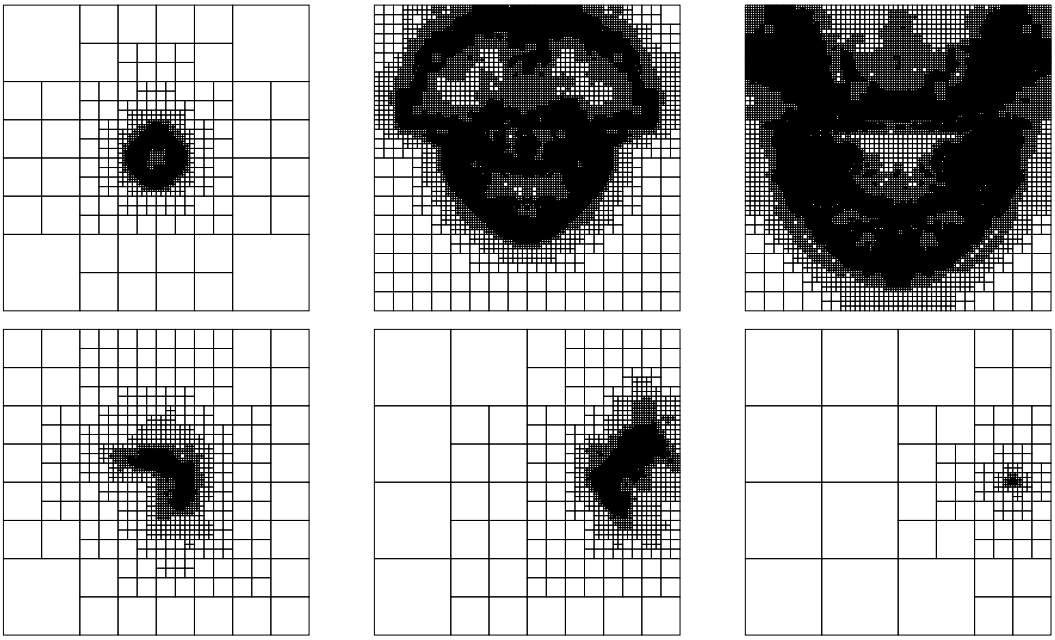

Figure 11: *Example 4. Top row: grids at times* $t = 0.15$, $t = 0.45$ *and* $t = T$, *with refinement by the simplified energy error indicator* (19). *Bottom row: grids produced by the dual estimator* (15). *All grids are after four cycles of refinement and coarsening.*

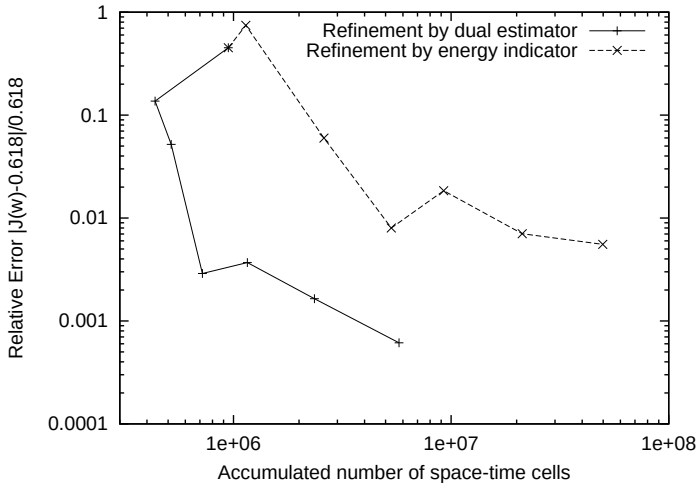

Figure 12: *Example 4. Convergence of the target functional* $J(\mathbf{w})$ *to the estimated exact value* 0.618. *Note that the dip in each curve are due to a change in the sign of the error.*

In Fig. 12 the convergence of the target functional $J(\mathbf{w}_h)$ towards the inferred value $J(\mathbf{w}) \approx 0.618$ is shown. Since the grids only tracked the interesting part of the wave it is not surprising that it accomplishes the same accuracy with a significantly lower number of space-time cells than the grids refined with the simplified energy error indicator (19).

Note that the dip in each curve is due to the error, $J(\mathbf{w}_h) - 0.618$, changing its sign, which happens to bring $J(\mathbf{w}_h)$ close to the exact value. Leaving aside these two data points, the grids as refined by (15) show a higher order of convergence than the grids as refined by (19). It should be mentioned that refinement by the two methods starts from the same grid, but that in the first step the error estimator (15) coarsens more cells than it refines, which leads to an overall decrease of space-time cells.

5 Conclusions

In this paper, an approach has been presented to solving the acoustic wave equation by an adaptive finite element method including a posteriori error control in physically meaningful quantities. Refinement of the grid is based on a representation of the exact error with respect to an arbitrary functional of the solution, which includes the local residuals of the numerical solution and local weights derived from the solution of a dual problem which is adjusted to the quantity of interest.

It was shown that meshes generated with the aid of refinement criteria derived from this error identity are significantly superior to meshes obtained by a simplified refinement indicator which does not include information on the quantity of interest. The superiority was demonstrated with several examples of one and two dimensional wave propagation, including high frequency waves and discontinuous coefficients. In particular, it was shown that refinement based on the error representation is able to track where information comes from, thus leading to highly localized grid refinement if the target functional is localized. In general, the smaller the region of evaluation of the target functional is, the larger are the savings of the new approach presented here compared to global refinement and to more traditional approaches of adaptivity.

Furthermore, it was shown that using the approach presented here, quantitative error control is feasible. Using a complex example of one dimensional wave propagation, the estimated error tracked the true error within a range of less than a factor of two. Additionally, the indicated error correctly predicted the sign of the error.

Finally, several aspects of the underlying mechanisms have been investigated into, as well as alternatives of the evaluation of the error representation formula. It was shown that good mesh refinement criteria including the localized information about the target functional can be obtained by computing the dual problem to the same accuracy as the primal one. This doubles the computational cost compared to the pure forward solution, but usually reduces the computing work by at least an order of magnitude compared to simple ad hoc approaches to adaptivity, due to the more economical meshes produced.

References

[1] L. Bales and I. Lasiecka. Continuous finite elements in space and time for the nonhomogeneous wave equation. *Computers Math. Applic.*, 27(3):91–102, 1994.

[2] W. Bangerth. Adaptive Finite-Elemente-Methoden zur Lösung der Wellengleichung mit Anwendung in der Physik der Sonne. Diplomarbeit, Institut für Angewandte Mathematik, Universität Heidelberg, 1998.

[3] W. Bangerth, R. Hartmann, and G. Kanschat. `deal.II` *Differential Equations Analysis Library, Technical Reference*, 2004. `http://www.dealii.org/`.

[4] W. Bangerth and G. Kanschat. Concepts for object-oriented finite element software – the `deal.II` library. Preprint 99-43, SFB 359, Universität Heidelberg, Oct. 1999.

[5] Z. P. Bažant. Spurious reflection of elastic waves in nonuniform finite element grids. *Comput. Methods Appl. Mech. Engrg.*, 16:91–100, 1978.

[6] R. Becker and R. Rannacher. A feed-back approach to error control in finite element methods: Basic analysis and examples. *East–West J. Numer. Math.*, 4:237–264, 1996.

[7] R. Becker and R. Rannacher. Weighted a posteriori error control in FE methods. In e. a. H. G. Bock, editor, *ENUMATH 95*, pages 621–637, Paris, September 1998. World Scientific Publ., Singapure. in [8].

[8] H. G. Bock, F. Brezzi, R. Glowinsky, G. Kanschat, Y. A. Kuznetsov, J. Priaux, and R. Rannacher, editors. *ENUMATH 97, Proceedings of the 2nd European Conference on Numerical Mathematics and Advanced Applications*, Singapore, 1998. World Scientific.

[9] P. G. Ciarlet. *The Finite Element Method for Elliptic Problems*, volume 4 of *Studies in Mathematics and its Applications*. North-Holland, Amsterdam, New York, Oxford, first edition, 1978.

[10] K. Eriksson, D. Estep, P. Hansbo, and C. Johnson. Introduction to adaptive methods for differential equations. *Acta Numerica*, pages 105–158, 1995.

[11] K. Eriksson and C. Johnson. An adaptive finite element method for linear elliptic problems. *Math. Comp.*, 50:361–383, 1988.

[12] D. A. French and T. E. Peterson. A continuous space-time finite element method for the wave equation. *Math. Comp.*, 65:491–506, 1996.

[13] I. Harari. Reducing spurious dispersion, anisotropy and reflection in finite element analysis of time-harmonic acoustics. *Comput. Methods Appl. Mech. Engrg.*, 140:39–58, 1997.

[14] R. Hartmann. A posteriori Fehlerschätzung und adaptive Schrittweiten- und Ortsgittersteuerung bei Galerkin-Verfahren für die Wärmeleitungsgleichung. Diplomarbeit, Institut für Angewandte Mathematik, Universität Heidelberg, 1998.

[15] G. Hulbert. Time finite element methods for structural dynamics. *Inter. J. Numer. Methods Engrg.*, 33:307–331, 1992.

[16] G. M. Hulbert and T. J. R. Hughes. Space-time finite element methods for second-order hyperbolic equations. *Comput. Methods Appl. Mech. Engrg.*, 84:327–348, 1990.

[17] C. Johnson. *Finite Element Methods for Partial Differential Equations*. Cambridge University Press, 1993.

[18] G. Kanschat. Solution of multi-dimensional radiative transfer problems on parallel computers. In P. Bjørstad and M. Luskin, editors, *Parallel Solution of Partial Differential Equations*, volume 120 of *IMA Volumes in Mathematics and its Applications*, pages 85–96, New York, 2000. Springer.

[19] D. W. Kelly, J. P. d. S. R. Gago, O. C. Zienkiewicz, and I. Babuška. A posteriori error analysis and adaptive processes in the finite element method: Part I–error analysis. *Int. J. Num. Meth. Engrg.*, 19:1593–1619, 1983.

[20] X. D. Li and N.-E. Wiberg. Implementation and adaptivity of a space-time finite element method for structural dynamics. *Comput. Methods Appl. Mech. Engrg.*, 156:211–229, 1998.

[21] J. T. Oden and S. Prudhomme. Goal-oriented error estimation and adaptivity for the finite element method. TICAM Report 99–15, University of Texas, Austin, Apr. 1999.

[22] J. Peraire and A. T. Patera. Bounds for linear-functional outputs of coercive partial differential equations: Local indicators and adaptive refinement. In P. Ladevèze and J. T. Oden, editors, *Proceedings of the Workshop on Advances in Adaptive Computational Methods in Mechanics, Cachan, 17–19 September 1997*, pages 199–216. Elsevier, 1998.

[23] R. Rannacher and F.-T. Suttmeier. A feed-back approach to error control in finite element methods: Application to linear elasticity. *Comp. Mech.*, 19(5):434–446, 1997.